

Influence of Periodic-Blowing Actuators on the Wake and the Total Drag of Generic 3D Car Models

Daniel Krentel^{1,*}, Rifet Muminovic^{2,*}, Wolfgang Nitsche and Rudibert King

¹Technische Universität Berlin, Department of Aeronautics and Astronautics, Chair of Aerodynamics, Marchstr. 12, D-10587 Berlin, Germany

²Technische Universität Berlin, Department of Process Engineering, Chair of Measurement and Control, Hardenbergstr. 36a, D-10623 Berlin, Germany

Received date 23rd February 2012; Accepted date 26th December 2012

ABSTRACT

Within the scope of the Collaborative Research Centre SFB 557 “Control of Complex Turbulent Shear Flows” at TU Berlin this project deals with the reduction of the total drag of generic three-dimensional car models (Ahmed body) by means of Active Flow Control (AFC). The highly complex wake region behind these models consists of steady longitudinal vortices occurring at the outer slant edges depending on the slant angle and unsteady lateral vortex structures occurring at the upper and lower edge of the base between the longitudinal structures. During the experiments these vortex structures were influenced by different actuation concepts using steady- and periodic-blowing compressed-air jets. A variation of the forcing intensity and frequency (Strouhal number) showed a strong influence of these parameters on the effectiveness of the actuation. The isolated use of the different actuation concepts leads to a drag reduction of up to 5.6% (steady blowing) or 5.1% respectively (periodic-blowing slot). The combination of the two actuation concepts enables a drag reduction of up to 7.1% and an increase in base pressure of up to 15.5%. An extremum-seeking feedback controller was used to exploit the full AFC benefits, e. g. the controller adjusts the optimal actuation parameters, such that the total drag is minimized.

1. INTRODUCTION

Active Flow Control is a suitable measure to reduce the pressure drag as the dominating drag component of bluff bodies next to passive methods. This drag component is mostly defined by the flow separation at the rear end of these models resulting in a static pressure difference between the front and the rear end of these models. Preceding experimental investigations frequently utilized the so-called Ahmed body geometry introduced by S. R. Ahmed et al. [1] representing a generic car model. The flow field behind this generic configuration depicted in Fig. 1(a) is very complex, three-dimensional and unsteady. The topology of the recirculation area strongly depends on the slant angle ϕ (compare Fig. 1). The increase in total drag with increasing slant angle up to $\phi \approx 30^\circ$ is caused by large stable longitudinal vortex structures occurring at the lateral slant edges. For slant angles exceeding this critical angle these vortex structures burst and thus lateral vortex structures dominate the flow field composing to two counter-rotating vortices in the time-averaged depiction of the symmetry plane (Fig. 3).

The successful application of Active Drag Control on different bluff body configurations using compressed-air actuators was already presented by Brunn et al. [2, 3] and Krentel et al. [4]. Using a steady-blowing approach near the slant corners mitigating the longitudinal vortices Brunn et al. [2] achieved a drag reduction of up to 2.5% and 25° Ahmed body. Krentel et al. generated a drag reduction of up to 5.7% ($\phi = 25^\circ$) and 2.2% ($\phi = 90^\circ$) using periodic-blowing slot actuators situated at the slant edges of the Ahmed bodies with different jet angles. The investigated drag reductions were always consistent with a considerable increase in static base pressure which is an indicator for a decrease in

*Corresponding authors, Email: daniel.krentel@ilr.tu-berlin.de; rifet.muminovic@tu-berlin.de

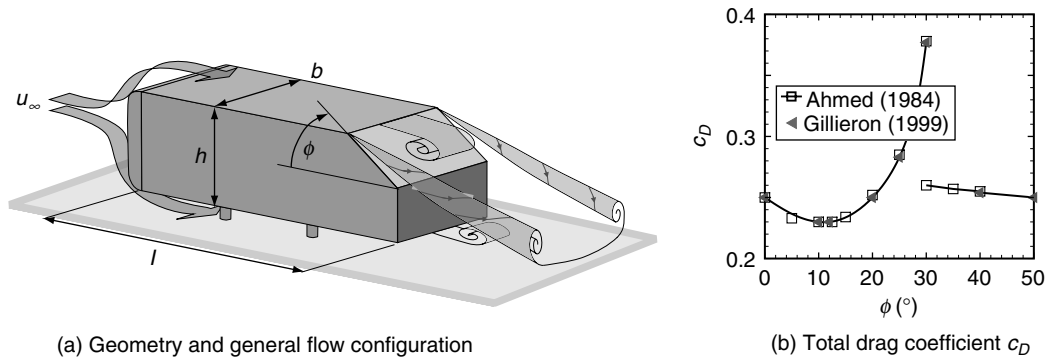


Figure 1. Ahmed body [2].

pressure drag. Krentel et al. [4, 5] proved the induction of stable large-scale vortex structures near the model base by the actuator jet using time-resolved *Particle Image Velocimetry* measurements (TR-PIV). These vortices lead to a considerable increase in turbulent momentum exchange, which was investigated by Brunn et al. [3] as well using hot-wire anemometry. For the steady-blowing actuator at the 25° slant configuration Krentel et al. [4] implemented a model-predictive closed-loop control scheme facilitating a good reaction to flow disturbances like sudden changes in the flow velocity leading to a change in the Reynolds number. Numerical approaches presented by Rouméas et al. [6], Wassen et al. [7] or Krajnović et al. [8] achieved even higher drag reduction using different actuation concepts.

This paper presents further investigations on Active Drag Control applied to an Ahmed body with a slant angle of 25°. The combined actuation using two different actuation systems leads to a further drag reduction. Additionally closed-loop control approaches are investigated improving the performance and applicability of the active measures.

2. EXPERIMENTAL SET-UP

The experiments were conducted in the closed test section (width $b_{TS} = 600$ mm, height $h_{TS} = 400$ mm) of a closed-loop low-speed wind tunnel using a 1:4-scaled model of the Ahmed body (length $l = 261$ mm, width $b = 97$ mm, height $h = 72$ mm) with a slant angle of $\phi = 25^\circ$. The model-length based Reynolds number was set to $Re = 0.46 \times 10^6$ for the open-loop control experiments. The three-dimensional model was mounted with four struts on a strain gauge drag balance that was situated under the wind tunnel floor. The distance between the wind tunnel floor and the bluff body was approximately 12.5 mm.

Additionally to the drag measurements the local static pressure at the rear end of the model was measured at 4 (slant) and 5 (base) different positions using amplified differential pressure sensors on a piezo-resistive base (compare Fig. 2, pressure taps 1 to 9). Next to this the model was equipped with 4 actuators at different positions. Near the slant corners of the model two steady-blowing slots S1 each consisting of three holes were installed with a nominal jet direction perpendicular to the undisturbed flow and slightly outward. Three periodic-blowing slot actuators P2 to P4 (slot dimensions: $l_s \times b_s = 80$ mm \times 0.1 mm) were integrated at the three edges of the rear end with a nominal jet angle of $\theta = 45^\circ$ relative to the undisturbed flow; this jet angle slightly shifts with increasing mass flow. The forcing intensity c_μ (Eq. 1) was controlled by one proportional pressure regulator for each actuator (Amplitude p_{amp}). The airflow to the slot actuators P2 to P4 was furthermore controlled by fast switching solenoid valves regulating the duty cycle (used here: 50%) and the dimensionless actuation frequency Sr (Eq. 2). The additional thrust or drag force resulting from the actuator jets is accounted for in the presented results. The correction of the blockage effect of the model due to the closed test section was accomplished according to the method of Mercker described in [9]. For this model an overall blockage factor of 1.039 resulted covering the effect of solid and wake blockage. The laminar-turbulent transition was fixed at approximately 11% of the model length using a serrated velcro strip.

The following definition of the momentum coefficient as a dimensionless parameter for the forcing intensity is used:

$$c_\mu = \frac{A_{act}}{A_m} \times \left(\frac{\overline{c'_{act}}}{U_\infty} \right)^2, \quad (1)$$

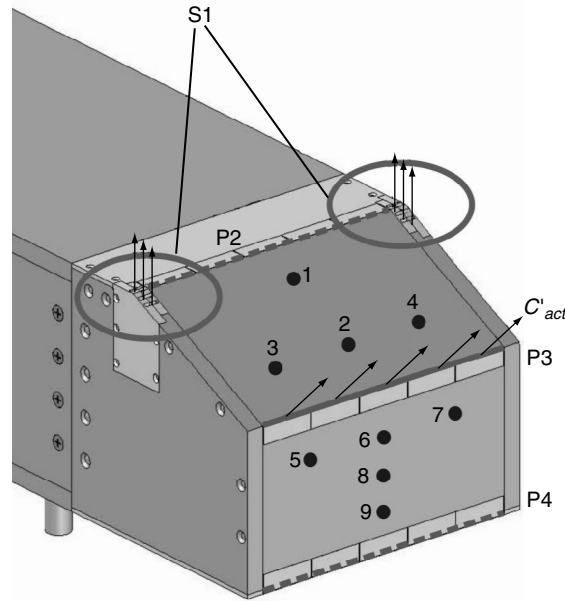


Figure 2. Rear end of Ahmed body with actuators (S1, P2 to P4) and pressure taps (1 to 9).

with the active actuator area $A_{act} = l_s \times b_s$, the area cross-section of the model $A_m = b \times h$, the mean perturbation velocity at the actuator slot exhaust \bar{c}'_{act} and the average velocity of the undisturbed flow U_∞ . The perturbation velocity of the actuator jet c'_{act} corresponding to a specific primary pressure p_{ampl} was measured using a hot wire probe and *Constant Temperature Anemometry* (CTA).

In the following chapters the Strouhal number Sr as a dimensionless actuation frequency will be used based on the height of the bluff body h as a characteristic length scale for the recirculation region:

$$Sr = \frac{f \times h}{U_\infty}. \quad (2)$$

For the statistical evaluation of hot-wire anemometry data the common definitions of the central moments are used:

$$\text{Standard deviation: } \sqrt{\mu_2} = \sigma = \sqrt{\frac{1}{N-1} \sum_{n=1}^N [S_n(t) - \bar{s}]^2} \quad (3)$$

$$\text{Skewness: } \mu_3 = \frac{1}{N} \sum_{n=1}^N \frac{[S_n(t) - \bar{s}]^3}{\sigma^3} \quad (4)$$

$$\text{Kurtosis: } \mu_4 = \frac{1}{N} \sum_{n=1}^N \frac{[S_n(t) - \bar{s}]^4}{\sigma^4} \quad (5)$$

3. RESULTS

3.1. Base Flow

The base flow was investigated in an additional water tunnel experiment at a Reynolds number of $Re = 0.5 \times 10^6$ using a *Particle Image Velocimetry* system. Figure 3 shows the complete wake region behind the rear end of the 1:4-scaled Ahmed body in a time-averaged depiction of the symmetry plane. The separated flow at the base edges generates a ring vortex which is depicted as two counterrotating lateral vortices forming the wake region in the cross-section of Fig. 3. The separation length is approximately 70% of the model height h . The influence of the longitudinal vortices is not directly detectable in the symmetry plane.

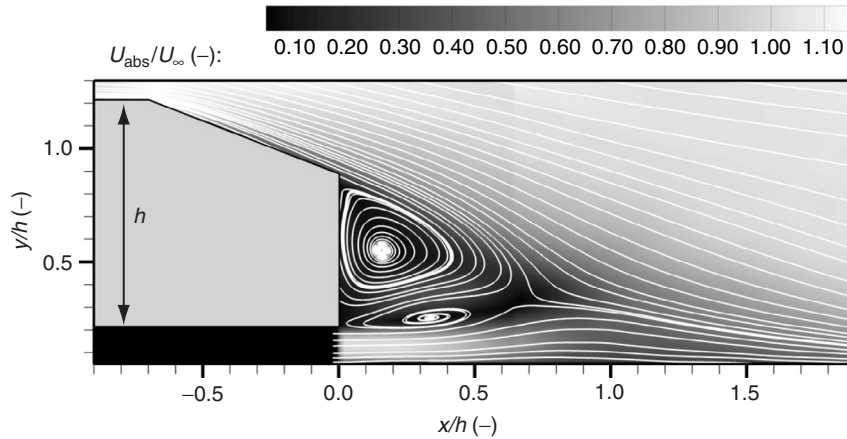


Figure 3. Time-averaged flow field around the rear end of the Ahmed body (baseflow, symmetry plane, water tunnel experiment, $Re = 0.5 \times 10^6$).

3.2. Forced Flow

In this section results for the actuated flow using the steady-blowing actuators S1, the periodic-blowing actuator P3 and a combination of both are presented. The isolated use of the steady-blowing actuators S1 presented in Fig. 4(a) leads to drag reductions of up to 5.6% depending on the forcing intensity. The forcing produces contrary effects on the mean slant and pressure: While the static pressure on the base is considerably increased with rising forcing amplitude, the mean static slant pressure decreases. Thus the drag-decreasing effect of the steady-blowing jet can be traced back to a pressure gain on the model base. This indicates that the mitigation of the longitudinal corner vortices using the steady-blowing actuators leads to a change of the topology of the recirculation region behind the model base compared to the base flow; the influence of the corner vortices on the wake is considerably decreased. The impact of the dimensionless forcing frequency Sr of actuator P3 on the possible drag reduction with a constant momentum coefficient of $c_{\mu} = 1.1 \times 10^{-5}$ ($p_{ampl} = 1 \text{ bar}$) is presented in Fig. 4(b). The actuation with low-frequent compressed-air jets leads to a drag reduction of up to 3.6%. The upstream mean slant pressure is increased by up to 21%, in contrast to the static base pressure here hardly any influence of the actuation frequency is detectable. The isolated periodic blowing using actuator P3 causes a considerable decrease in base pressure for all investigated Strouhal numbers without any apparent saturation effect with increasing frequency. The positive effect of the periodic-blowing jet can be traced back exclusively to an increase in slant pressure for small Strouhal numbers in the range of $Sr = 0.05$, when the loss in base pressure does not exceed the pressure gain on the slant.

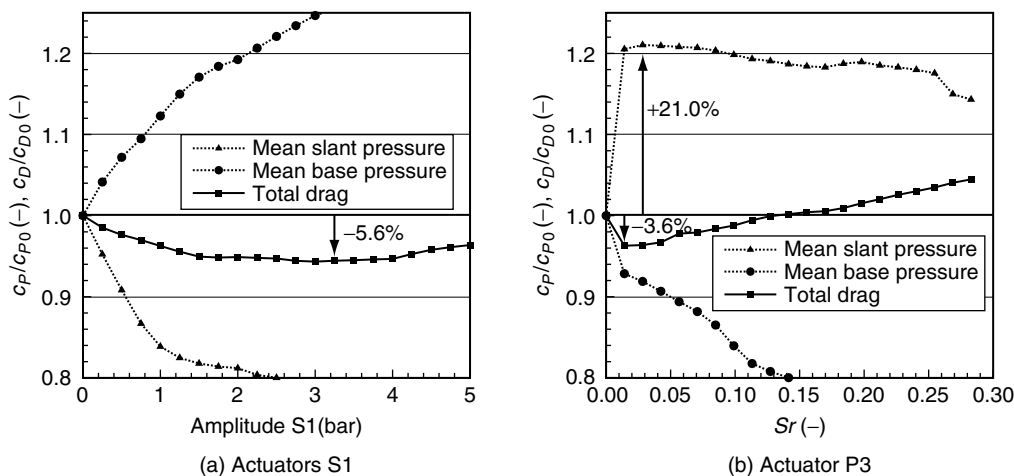


Figure 4. Influence of isolated forcing (actuators S1 or P3) on the total drag and the relative mean static pressure coefficient of the slant and the base.

Figure 5 presents a comparison between isolated periodic-blowing forcing (P3 only) and a combination of the actuators S1 and P3. The best drag reduction of 5.1% using P3 only is achieved with an optimal forcing frequency for actuator P3 of $Sr = 0.02$ (momentum coefficient of $c_\mu = 2.6 \times 10^{-4}$, Amplitude $p_{ampl} = 3 \text{ bar}$). When the longitudinal vortices are mitigated before using the steady-blowing actuators S1 (with $p_{ampl} = 3 \text{ bar}$, combined actuation S1 and P3) the momentum coefficient for the periodic blowing can be reduced significantly ($c_\mu = 1.1 \times 10^{-5}$, Amplitude $p_{ampl} = 1 \text{ bar}$), whereas the overall possible drag reduction increases to 7.1%. In Fig. 5(b) the influence of the actuation on the mean static slant and base pressure is depicted. A significant increase in base pressure (of up to 15.5%) without negative effect on the slant can only be achieved using the combined actuation. This clarifies the importance of a preceding actuation of the longitudinal vortices to increase the effectiveness of the periodic blowing; thus the combined actuation is necessary to perform an optimal forcing.

Figure 6 indicates the influence of the periodic-blowing jet on the frequency spectrum of the shear layer behind the model base (measured at position $\frac{x}{h} = 0.14$, $\frac{y}{h} = 0.79$) compared to the baseflow. The

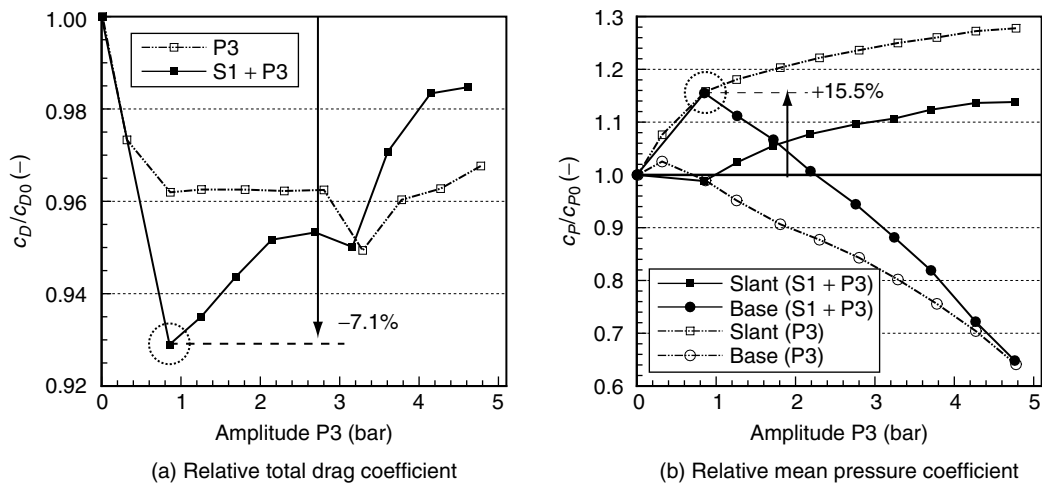


Figure 5. Influence of steady-blowing (S1, $p_{ampl,S1} = 3 \text{ bar}$) and periodic-blowing (P3, $Sr = 0.02$) actuation on the total drag and the mean static pressure coefficient.

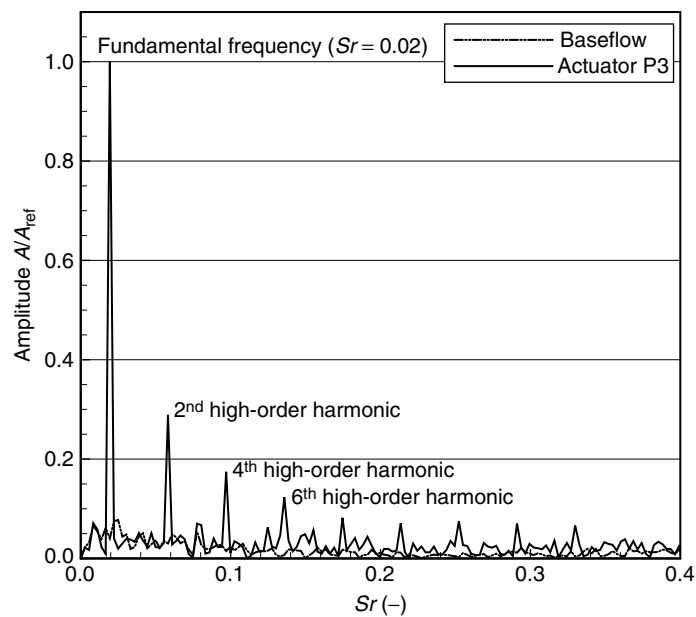


Figure 6. Frequency spectra of the shear layer behind the model for two different cases (position $\frac{x}{h} = 0.14$, $\frac{y}{h} = 0.79$. compare Figs. 3 and 9(a) for orientation).

baseflow contains a broad spectrum of predominantly low-frequent flow structures. Compared to that the periodic-blowing case with an optimal dimensionless actuation frequency of $Sr = 0.02$ is dominated by the actuator frequency, sharp peaks representing the fundamental actuation frequency and high-order harmonics can be clearly identified in the spectrum. Thus the excited shear layer emanating from the upper base edge contains strong flow structures with the forcing frequency. Due to the square wave signal applied to the solenoid valve only every second high-order harmonic is present in the spectrum.

The periodic-blowing jet has an up- and downstream effect on the flowfield. Figure 7 presents the time traces of two pressure taps (Pos. 2 and 6, compare Fig. 2) in the vicinity of slot P3. On the slant (Pos. 2) the pressure coefficient increases from approximately -0.27 to -0.12 with a short delay when the actuator is active. On the upper part of the base (Pos. 6) in contrast the static pressure is decreased considerably (pressure coefficient reduced from -0.20 to -0.28) when the actuator emits fluid. The dashed line represents the trigger signal handed over to the fast switching solenoid valve controlling actuator P3.

The aforementioned forced periodic flow structures in the shear layer induce a strong increase in the turbulent velocity fluctuation. Figure 8 depicts the difference of the standard deviation of the absolute velocity relative to the standard deviation of the baseflow case in the wake region behind the Ahmed body for three actuation cases. The increased velocity fluctuations indicate an augmentation of the turbulent momentum exchange between the shear layer and the outer flow described by Brunn et al. [3]. For the combined actuation (S1 and P3) the wake region with an increased fluctuation intensity considerably exceeds the two isolated forcing cases.

A statistical analysis of the hot-wire data in the symmetry plane at a distance of $\frac{x}{h} = 0.14$ ($x = 10$ mm) from the model base is depicted in Fig. 9. The velocity profiles in Fig. 9(a) show a minor influence of the different actuators. The steady-blowing actuators S1 (isolated and in combination with P3) cause a decrease in velocity around the lower part of the model base (between approximately $\frac{y}{h} = 0.2$ and $\frac{y}{h} = 0.5$) compared to the base flow. This decrease in velocity is consistent with the increase in static pressure depicted in Fig. 4(a) and Fig. 5(b). There can be hardly any characteristic effect of the periodic jet P3 on the mean velocity profile detected. Compared to that the periodic jet P3 can be identified as a strong peak in the relative standard deviation depicted in Fig. 9(b). The jet causes the aforementioned increase in velocity fluctuation. In contrast the steady-blowing actuator leads to a flow field with less velocity perturbations near the model base. The skewness in Fig. 9(c) presents further statistical results concerning the two characteristic areas (between $\frac{y}{h} = 0.2$ and $\frac{y}{h} = 0.5$ and the jet at approximately $\frac{y}{h} = 0.82$). The sharply bounded region influenced by the periodic-blowing jet P3 has a negative skewness implying an asymmetric spreading of the velocity values shifted to higher values. The lower part of the base in contrast is defined by a considerable positive skewness when the steady blowing is activated, thus smaller values

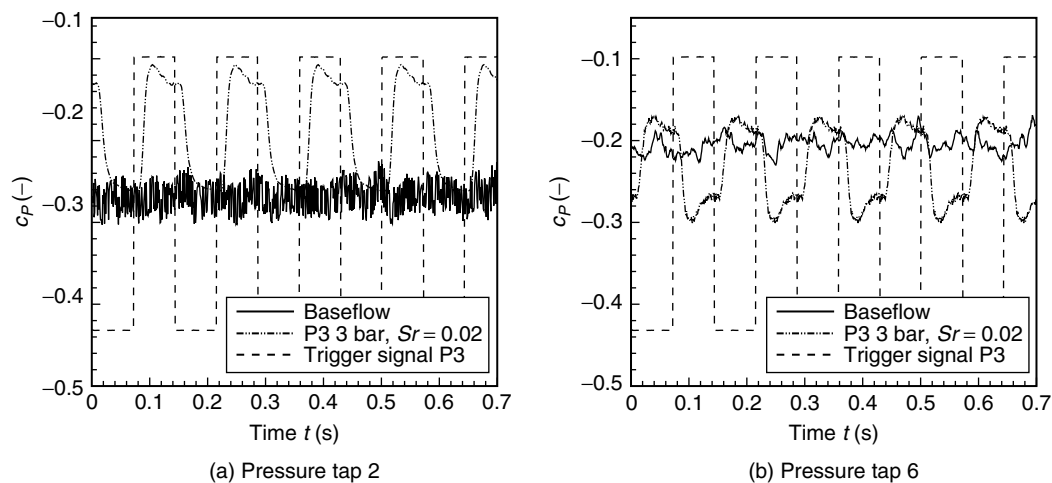


Figure 7. Influence of periodic-blowing jet P3 on the time-resolved static pressure coefficient (forced case: phase-averaged).

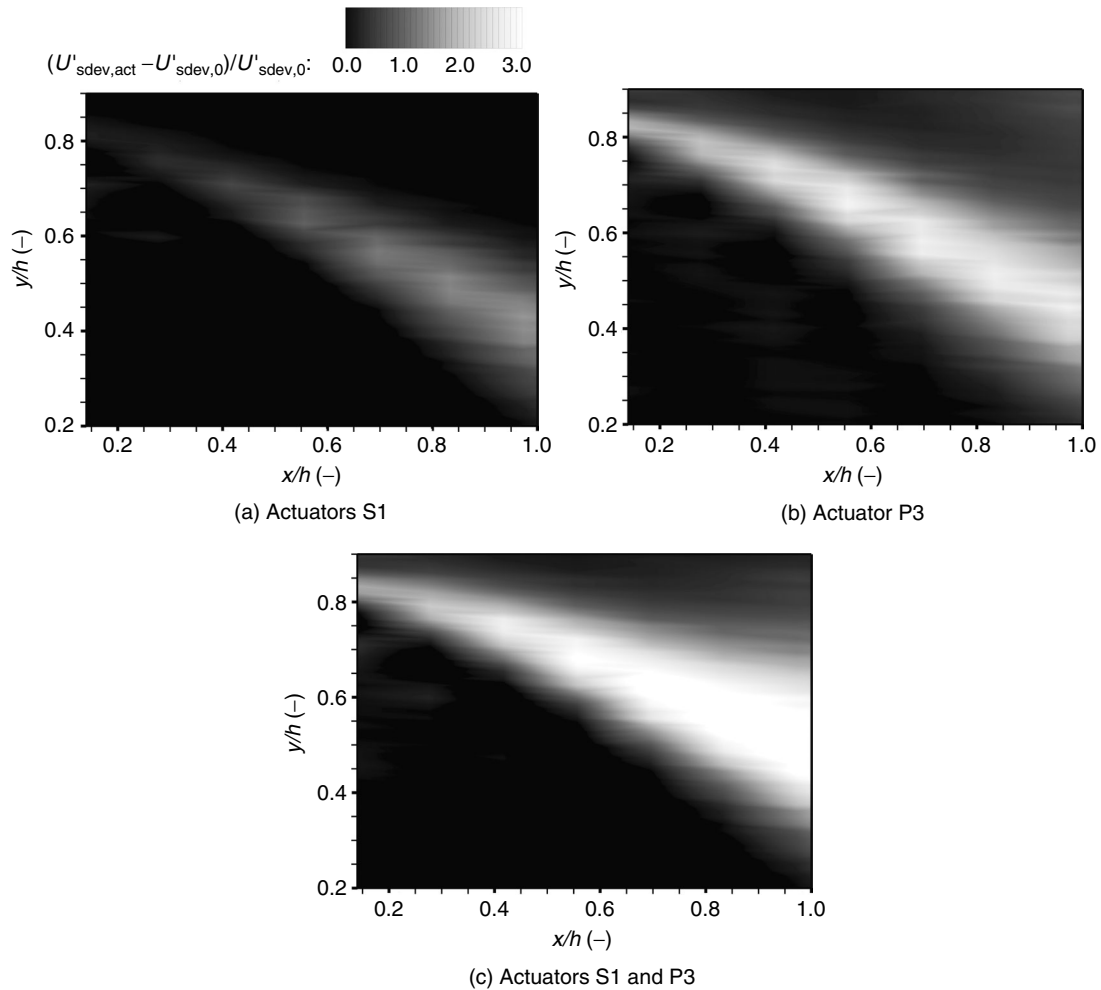


Figure 8. Relative difference of standard deviation σ of the absolute velocity U in the flow field behind the model for different actuation cases (symmetry plane, actuators S1: $p_{ampl} = 3$ bar, actuator P3: $p_{ampl} = 1$ bar, $Sr = 0.02$).

dominate the asymmetric distribution compared to the symmetric Gaussian distribution ($\mu_3 = 0$).

The central moment of fourth order, the kurtosis presented in Fig. 9(d), provides information about the steepness of the velocity distribution. The Gaussian distribution has a kurtosis of 3, higher values lead to a more and more narrow peak, while smaller values broaden the peak and imply less distinctive maxima of the distribution. The outflow at a dimensionless height $\frac{y}{h} > 1.0$ has a low degree of turbulence (compare Fig. 9(b), standard deviation) and thus a very distinctive maximum resulting in a very high kurtosis. In the shear layer that is affected by the periodic-blowing jet P3 the kurtosis is minimized so that the maximum is considerable broad compared to the distribution of the baseflow. The decelerated flow at the lower part of the base (due to the influence of steady blowing, S1) is defined by a low velocity fluctuation (compare Fig. 9(b), standard deviation) and a locally maximized kurtosis leading to a more distinctive velocity peak. The statistical analysis of the hot-wire data proves that a combination of the steady blowing (S1) and the periodic blowing (P3) features both effects of the different forcing methods on the recirculation area and the separated shear layer with only a minor mutual interference. Thus a combination enables further possibilities to reduce the total drag compared to isolated forcing.

3.3. Closed-Loop Control

In this research study closed-loop controllers are used to reduce the total drag of the Ahmed body. Extremum-seeking controllers with an extended Kalman filter for an estimation of the local gradient are implemented and tested in experiments. In Sect. 3.3.1 an introduction to the extremum-seeking

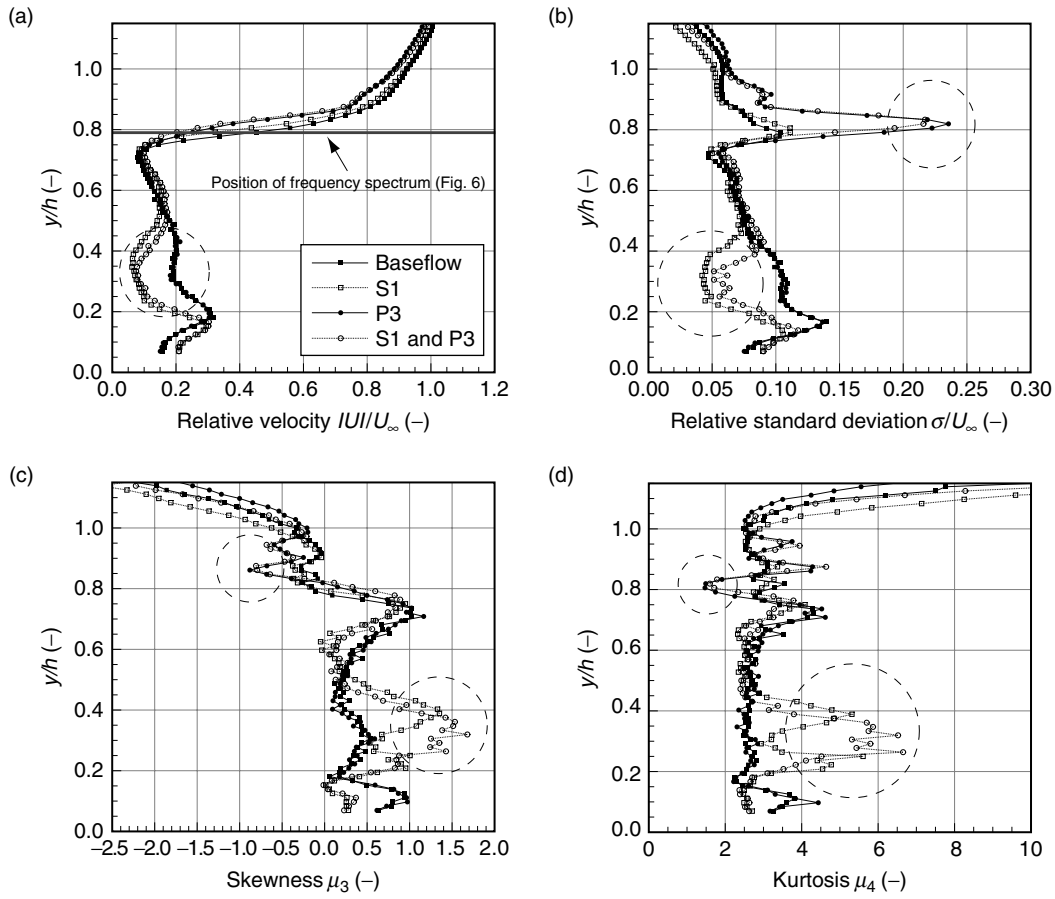


Figure 9. Results of hot-wire measurements in the symmetry plane behind the model (position $\frac{x}{h} = 0.14$ behind model base; actuators S1: $p_{amp1} = 3 \text{ bar}$; actuator P3: $p_{amp1} = 1 \text{ bar}$, $Sr = 0.02$).

controller is given. Afterwards the experimental results are presented in Sect. 3.3.2.

3.3.1. Extremum-Seeking Control

Extremum-seeking feedback control (ESC) is an adaptive, gradient-based and model-independent feedback scheme that searches for optimal actuation parameters (see [10, 11, 12, 13, 14]). The block diagram of the implemented ESC for the SISO (*single input - single output*) case is shown in Fig. 10. As shown in the figure, the nonlinear process is represented by an unknown steady-state map and a dynamical model. In ESC the process input $u(t)$ is perturbed slowly and harmonically, resulting in an approximately harmonic deflection of the process output $y(t)$ from its steady-state value. Based on the reaction of the process output, the controller deduces how the mean control input has to change in order to drive the process towards the extremum $y_s^* = f(u_s^*)$ in the steady-state map.

In contrast to the classical ESC (e. g. [10, 11, 12]) an extended Kalman filter (EKF) is used here for the local gradient estimation, resulting in a faster and more accurate estimation (see [13, 14]). As can be seen in Fig. 10, the process input is defined as

$$u(t) = u_0 + a \times \sin(\omega t) + \Delta u(t), \quad (6)$$

where u_0 is an initial control input, $\Delta u(t)$ is the change in the mean control input and $a \times \sin(\omega t)$ is a sinusoidal perturbation with amplitude a and frequency ω . Assuming the period of the harmonic actuation is larger than the largest time constant of the dynamic model, the output of the process will also be approximately sinusoidal, initially centered around $y_0 = f(u_0)$. Based on the process input $u(t)$ and output $y(t)$, the tangent on the steady-state map, depicted in Fig. 11, is estimated via an EKF. For small perturbation amplitudes a and slowly varying process inputs $u(t)$, the output can be approximated by

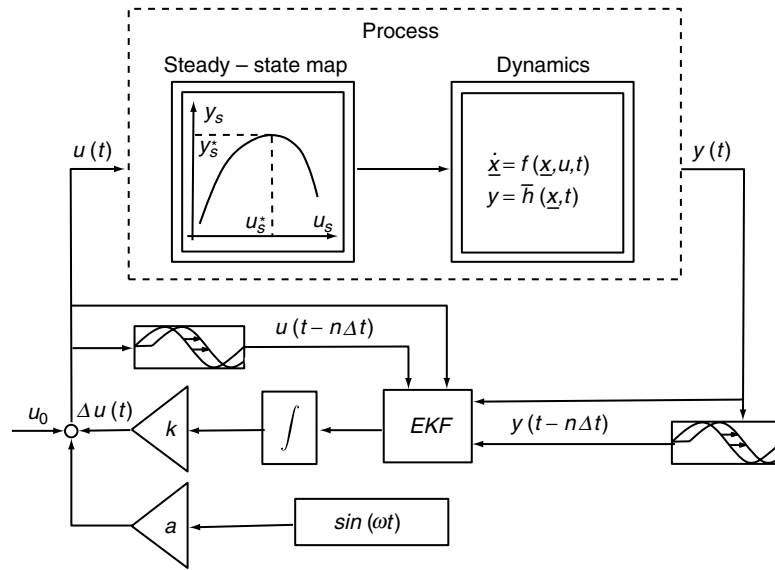


Figure 10. Block diagram of the closed-loop extremum-seeking controller with an extended Kalman filter (EKF) for local gradient estimation in the steady-state map.

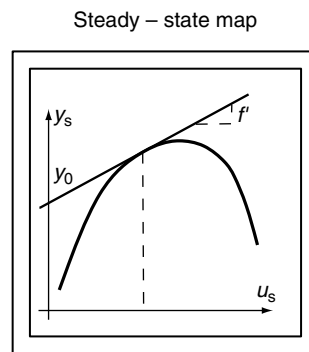


Figure 11. Steady-state map with tangent in current operating point.

$$y(t) \approx y_0 + f' \times a \times u(t), \tag{7}$$

where y_0 is the intersection with the y-axis and f' the local gradient of the tangent. As shown in [13] also time shifted versions of the process input $u(t)$ and the output $y(t)$ are needed in order to ensure observability. The estimated gradient f' is fed to an integrator and multiplied by a factor k , defining $\Delta u(t)$. For a more detailed explanation of the extremum-seeking controller and an extension to the DISO (dual input - single output) case the interested reader is referred to [13, 14].

3.3.2. Closed-Loop Control Results

The extremum-seeking controller has been applied in experiments in order to reduce the total drag of the Ahmed body. This section shows results with a SISO and a DISO extremum-seeking controller.

An experimental result with a SISO extremum-seeking controller is considered first. The Reynolds number based on the length of the Ahmed body is set to $Re = 0.4 \times 10^6$. The goal of the controller is to reduce the total drag. However, the drag is usually not directly measurable in real cars. Therefore the force $F_{x,p}$ resulting from the increase in slant and base pressure due to the actuation is used as a surrogate signal. Thus the resulting force $F_{x,p}$ is a force counteracting the drag. As shown in Fig. 12 the controller starts with an initial control input for the steady-blowing actuators S1 of $u_0 = 0.5$ and increases the mean control input from $\Delta u = 0$ to $\Delta u \approx 3.0$. The controller reaches the extremum in the

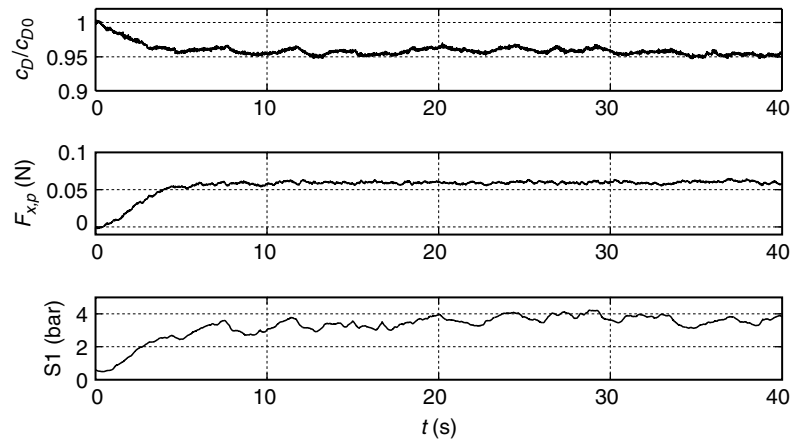


Figure 12. Experiment with a SISO extremum-seeking controller. The upper plot shows the total drag coefficient normalized with the total drag coefficient of the unactuated flow. The middle plot shows the mean force $F_{x,p}$ on the slant and the base of the body. The lower plot shows the control input.

steady-state map within 5 seconds, as can be seen in the force $F_{x,p}$. In the following only slight deviation due to the sinusoidal perturbations are visible. The normalized drag coefficient shows a total drag reduction of 5% (compare open-loop results, Sect. 3.2).

A second experiment with a DISO extremum-seeking controller was conducted. As can be seen in Fig. 13, the initial control inputs are $u_{0,1} = 0.8$ for S1 and $u_{0,2} = 4.0$ for P3. In the following, the controller increases S1 while simultaneously reducing P3, resulting in an increase in the force $F_{x,p}$. The controller takes approximately 35s to reach the extremum in the steady-state map. The DISO extremum-seeking controller is much slower compared to the SISO case because of the more complex

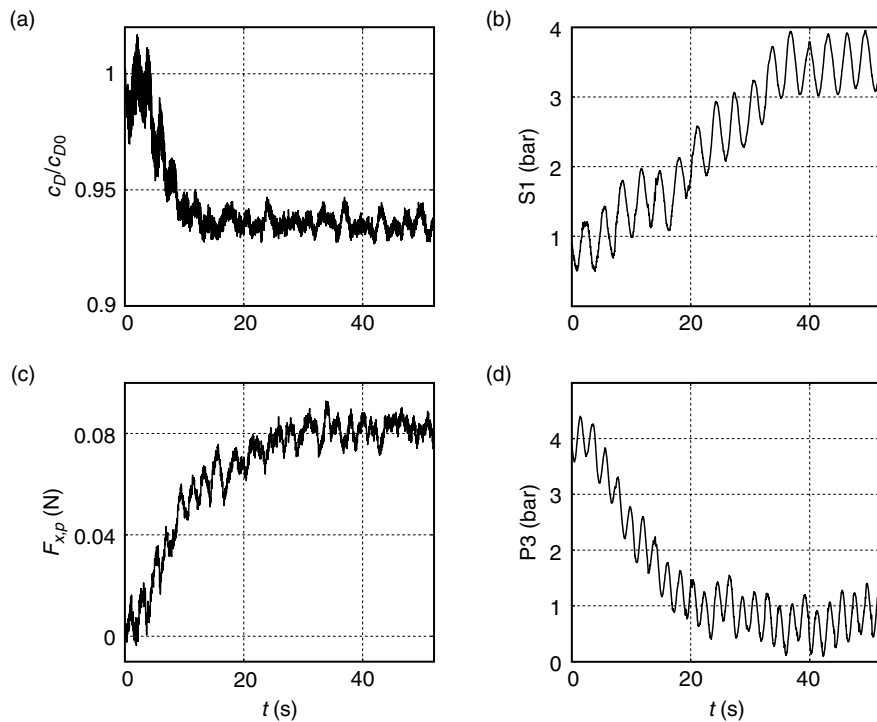


Figure 13. Experiment with a DISO extremum-seeking controller. The total drag coefficient normalized with the total drag coefficient of the unactuated flow is shown in (a). In (c) the mean force $F_{x,p}$ on the slant and the base of the body is depicted. In (b) and (d) the control inputs are shown.

gradient estimation. On the other hand, the increase in the force is higher compared to the SISO case, resulting in a reduction of 7% in the drag coefficient (compare open-loop results, Sect. 3.2). Both controllers show satisfactory performance. The main differences between them are the speed and the possible total drag reduction of the controllers. The SISO controller is faster whereas the DISO controller produces a higher drag reduction.

4. CONCLUSION

This study presents experimental results for an Active Drag Control approach on a bluff body configuration, the so-called Ahmed body with a slant angle of 25° , using a system of steady- and periodic-blowing compressed-air actuators at the rear end. The experiments were conducted in a closed test section with Reynolds numbers between $Re = 0.4 \times 10^6$ and $Re = 0.46 \times 10^6$. The separate use of the actuators enables drag reductions of up to 5.6% (steady blowing, mitigation of longitudinal vortices) and 5.1% (periodic blowing at the upper base edge) depending on the dimensionless forcing frequency (Strouhal number) and the forcing intensity (momentum coefficient). The different actuators have a contrary effect on the static slant and base pressure. A combination of the steady- and periodic-blowing jets leads to an optimal drag reduction of 7.1% consistent with an increase in mean base pressure of 15.5%. Further investigations are needed concerning the upstream effect of the periodic blowing on the slant and the complementary actuation using multiple periodic-blowing slots (e. g. at the lowerbase edge).

An investigation of the wake region in the symmetry plane using hot-wire anemometry provides details about the effect of the different actuation systems. The steady blowing decelerates the flow field near the lower part of the base and leads to a decrease in velocity fluctuations in this area. The periodic blowing in contrast increases the velocity fluctuations in the separated shear layer, this indicates an increase in turbulent mixing between the outer flow and the recirculation region. Next to this a *dual input-single output* (DISO) extremum-seeking controller using an extended Kalman filter was implemented varying the forcing intensity of two actuators to realize an optimal drag reduction.

The investigations show that it is crucial for a successful application of Active Drag Control to combine different actuation systems influencing different flow structures in the wake and recirculation region with the individual optimal forcing parameters (Strouhal number and momentum coefficient). Thus the application of closed-loop control is an essential instrument to implement an optimal Active Drag Control system.

ACKNOWLEDGEMENTS

This research was funded by the German Science Foundation (DFG) within the scope of the Collaborative Research Center SFB 557 “Control of Complex Turbulent Shear Flows”. This support is thankfully acknowledged by the authors. Steffen Kunze, Vincent Zander and Ralf Erdmann are gratefully acknowledged for their comments and advices on the experiments.

REFERENCES

- [1] Ahmed, S.R., Ramm, G.: Some Salient Features of the Time-Averaged Ground Vehicle Wake. SAE Technical Paper Series 840300, Society of Automotive Engineers (SAE) (1984).
- [2] Brunn, A., Wassen, E., Sperber, D., Nitsche, W., Thiele, F.: Active Drag Control for a Generic Car Model. In King, R., ed.: Active Flow Control. Volume 95 of Notes on Numerical Fluid Mechanics and Multidisciplinary Design (NNFM)., Springer (2007) 247–259.
- [3] Brunn, A., Nitsche, W.: Active control of turbulent separated flows over slanted surfaces. International Journal of Heat and Fluid Flow **27** (2006) 748–755.
- [4] Krentel, D., Muminovic, R., Brunn, A., Nitsche, W., King, R.: Application of Active Flow Control on Generic 3D Car Models. In King, R., ed.: Active Flow Control II. Volume 108 of Notes on Numerical Fluid Mechanics and Multidisciplinary Design (NNFM)., Springer (2010) 223–239.
- [5] Krentel, D., Haucke, F., Grund, T., Bauer, M., Hecklau, M., Nitsche, W.: Untersuchungen zur Interaktion gepulster Aktuatorjets mit abgelösten Scherschichten am Beispiel von Hochauftriebskonfigurationen und einem generischen Fahrzeugmodell mit Hilfe der zeitaufgelösten Particle Image Velocimetry. In: Lasermethoden in der Strömungsmesstechnik, 18. Fachtagung. (2010).
- [6] Rouméas, M., Gilliéron, P., Kourta, A.: Analysis and Control of the Near-wake Flow over a Square-back Geometry. Computers & Fluids **38** (2009) 60–70.

- [7] Wassen, E., Eichinger, S., Thiele, F.: Simulation of Active Drag Reduction for a Square-back Vehicle. In King, R., ed.: *Active Flow Control II*. Volume 108 of *Notes on Numerical Fluid Mechanics and Multidisciplinary Design (NNFM)*., Springer (2010) 241–255.
- [8] Krajnović, S., Östh, J., Basara, B.: LES of Active Flow Control around an Ahmed Body with Active Flow Control. In: *Conference on Modelling Fluid Flow (CMFF'09)*, The 14th International Conference on Fluid Flow Technologies, Budapest, Hungary, September 9–12 2009. (2009).
- [9] Cooper, K.R.: *Closed-test-section Wind Tunnel Blockage Corrections for Road Vehicles*. Special Publication SAE SP1176, Society of Automotive Engineers (SAE) (1996).
- [10] Morosanov, I.S.: Method of extremum control. *Automation Remote Control* **18** (1957) 1077–1092.
- [11] Beaudoin, J.F., Cadot, O., Aider, J.L., Wesfreid, J.E.: Drag reduction of a bluff body using adaptive control methods. *Physics of Fluids* **18** (2006) 1–10.
- [12] Ariyur, K., Krstic, M.: *Real-time optimization by extremum-seeking control*. John Wiley & Sons, Hoboken (2003).
- [13] Henning, L., Becker, R., Feuerbach, G., Muminovic, R., King, R., Brunn, A., Nitsche, W.: Extensions of adaptive slope-seeking for active flow control. *Proceedings of the Institution of Mechanical Engineers, Part I: Journal of Systems and Control Engineering* **222** (2008) 309–322.
- [14] Gelbert, G., Moeck, J.P., Paschereit, C.O., King, R.: Advanced algorithms for gradient estimation in one- and two-parameter extremum seeking controllers. Submitted to the *Journal of Process Control* (2010).